Short Article

Structure

Structure of the Human Mitochondrial Ribosome Studied *In Situ* by Cryoelectron Tomography

Graphical Abstract

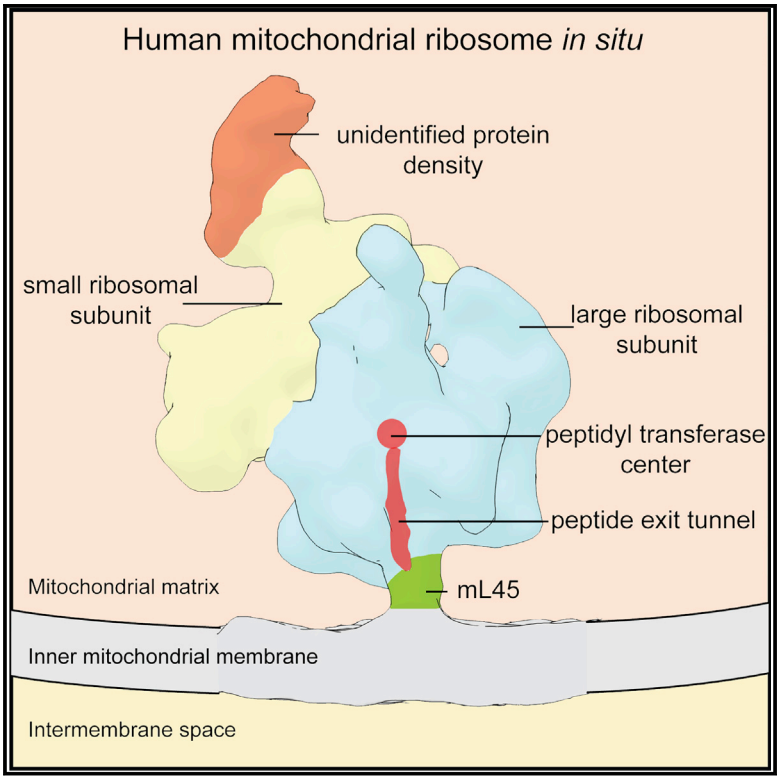

Highlights

- Human mitoribosomes are organized in clusters at the inner mitochondrial membrane
- An unidentified density is present at the small mitoribosomal subunit
- mL45 mediates the contact of human ribosome with the inner mitochondrial membrane
- The overall architecture of the mL45/Mba1 membrane contact is evolutionarily conserved

Authors

Robert Englmeier, Stefan Pfeffer, Friedrich Förster

Correspondence

f.g.forster@uu.nl

In Brief

Englmeier et al. employed cryoelectron tomography to determine the distribution and native structure of human mitoribosomes inside isolated mitochondria. The determined *in situ* structure of the membrane-bound human mitoribosome reveals its membrane interaction, an unidentified factor, and conserved features from yeast to human.

Englmeier et al., 2017, Structure *25*, 1574–1581
October 3, 2017
http://dx.doi.org/10.1016/j.str.2017.07.011

CellPress

Structure
Short Article

Structure of the Human Mitochondrial Ribosome Studied *In Situ* by Cryoelectron Tomography

Robert Englmeier,[1] Stefan Pfeffer,[2] and Friedrich Förster[1,2,3,*]
[1]Cryo-Electron Microscopy, Bijvoet Center for Biomolecular Research, Utrecht University, 3584 CH Utrecht, the Netherlands
[2]Max-Planck Institute of Biochemistry, Department of Molecular Structural Biology, 82152 Martinsried, Germany
[3]Lead Contact
*Correspondence: f.g.forster@uu.nl
http://dx.doi.org/10.1016/j.str.2017.07.011

SUMMARY

Mitochondria maintain their own genome and its corresponding protein synthesis machine, the mitochondrial ribosome (mitoribosome). Mitoribosomes primarily synthesize highly hydrophobic proteins of the inner mitochondrial membrane. Recent studies revealed the complete structure of the isolated mammalian mitoribosome, but its mode of membrane association remained hypothetical. In this study, we used cryoelectron tomography to visualize human mitoribosomes in isolated mitochondria. The subtomogram average of the membrane-associated human mitoribosome reveals a single major contact site with the inner membrane, mediated by the mitochondria-specific protein mL45. A second rRNA-mediated contact site that is present in yeast is absent in humans, resulting in a more variable association of the human mitoribosome with the inner membrane. Despite extensive structural differences of mammalian and fungal mitoribosomal structure, the principal organization of peptide exit tunnel and the mL45 homolog remains invariant, presumably to align the mitoribosome with the membrane-embedded insertion machinery.

INTRODUCTION

Mitochondria are organelles originating from bacteria that have been incorporated into eukaryotic cells in an endosymbiotic process. Throughout evolution, mitochondria maintained their own genome and protein synthesis machinery, including mitochondrial ribosomes (mitoribosomes). The human mitoribosome synthesizes 13 highly hydrophobic subunits of the oxidative phosphorylation (OxPhos) complexes I, III, IV, and V, which are co-translationally inserted into the inner mitochondrial membrane (IMM) (Ott and Herrmann, 2010). Mutations in these proteins are implicated in several diseases. Despite their importance for cellular function, little is known about the biogenesis of mitochondria-encoded proteins, e.g., their synthesis, concomitant membrane integration, and subsequent assembly into complexes.

Like their bacterial relatives, mitoribosomes are assembled from rRNA and ribosomal proteins. Throughout evolution the mitochondrial genome and, consequently, the mitochondrial rRNA changed drastically. Upon an initial constructive phase in protozoa characterized by the expansion of rRNA and the acquisition of novel proteins, metazoans went through a "destructive phase" with strong mitochondrial rRNA reduction and recruitment of further mitoribosome-specific proteins, giving rise to an inverted rRNA/protein ratio compared with bacterial ribosomes (van der Sluis et al., 2015). Recent studies of the mammalian and yeast mitoribosome by cryoelectron microscopy (cryo-EM) single-particle analysis (SPA) provided high-resolution insights into their structures and drastic variation throughout evolution. For example, the 73S yeast mitoribosome exhibits a completely remodeled peptide exit tunnel (Amunts et al., 2014), while this feature does not differ significantly between the bacterial ribosome and the mammalian mitoribosome (Greber et al., 2014). The consequences of the extensive mitoribosome evolution for the mechanism of translation, IMM association, and protein insertion remain unclear.

Co-translational insertion of nascent peptides into the IMM is most extensively studied in yeast. Genetic and biochemical studies identified two components of this process: the integral membrane protein Oxa1, which is thought to insert newly synthesized proteins into the IMM (Hell et al., 2001), and the IMM-associated mitoribosome receptor Mba1 (Lorenzi et al., 2016; Ott et al., 2006). Both proteins have homologs in mammals, Oxa1L and mL45, respectively. While Mba1 is absent in purified yeast mitoribosomes, mL45 is a constitutive mitoribosomal subunit in mammals, and its atomic structure in the context of the isolated human mitoribosome has been determined by cryo-EM SPA (Brown et al., 2014; Greber et al., 2014).

The association of the yeast mitoribosome with the native IMM has been studied *in situ* using cryoelectron tomography (CET) and subtomogram analysis (Pfeffer et al., 2015). The yeast mitoribosome associates with the IMM via two major contact sites, identified as the rRNA expansion segment 96-ES1 and Mba1, which binds near the ribosomal peptide exit tunnel (PET). In the mammalian 55S mitoribosome, 96-ES1 is absent and the PET has moved dramatically during evolution in yeast (Amunts et al., 2014, 2015; Greber et al., 2015; Pfeffer et al., 2015). Thus, the mode of membrane association remains to be addressed for the mammalian mitoribosome.

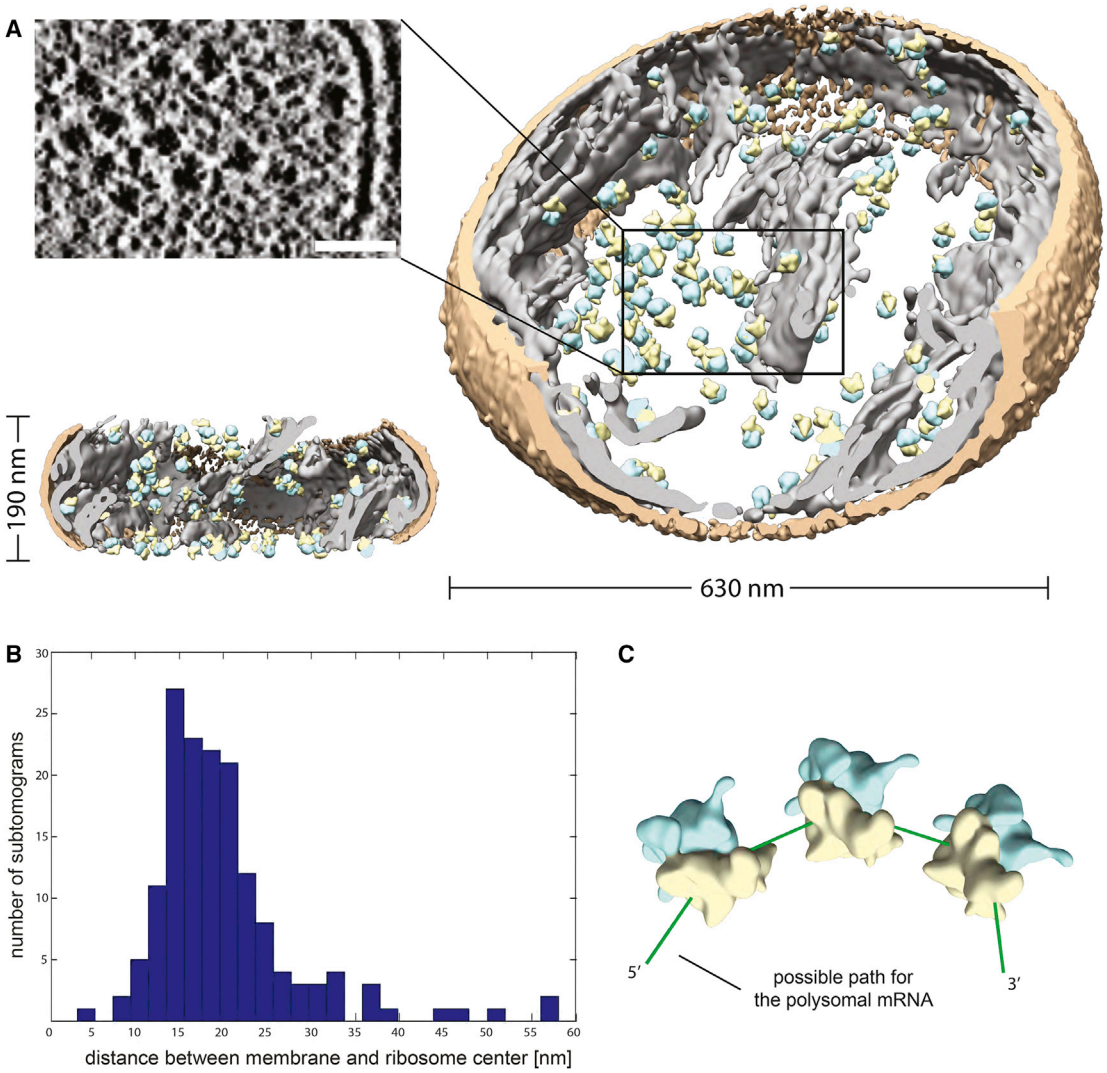

Figure 1. Distribution of Mitoribosomes Inside a Human Mitochondrion

(A) Distribution of mitoribosomes (LSU, blue; SSU, yellow) within a segmented mitochondrion (outer mitochondrial membrane [OMM], orange, IMM, gray). The slice of a tomogram (top left) depicts a cluster of mitoribosomes. Scale bar, 50 nm.

(B) Distribution of the center-to-membrane distances of 155 mitoribosomes from two tomograms.

(C) Average 3D arrangement of mitoribosomes in membrane-bound human mitochondrial polysomes, with a possible pathway for polysomal mRNA depicted in green. The membrane resides in the paper plane.

See also Figures S1 and S2.

Visualization of mitoribosomes within intact mitochondria is more challenging for mammals than for other previously studied organisms such as *Saccharomyces cerevisiae* (Pfeffer et al., 2015). The mammalian mitoribosome's low RNA/protein ratio and its smaller size causes comparably low contrast in the dense mitochondrial matrix, preventing their accurate detection in tomograms acquired using conventional defocus-induced phase-contrast CET. Here, we made use of the recently developed Volta phase plate (VPP) (Khoshouei et al., 2017) to increase contrast in CET and study the mammalian mitoribosome *in situ*. Using CET and subtomogram analysis, we studied the distribution and structure of human mitoribosomes in the context of the native IMM.

RESULTS

Distribution of Mitoribosomes in Human Mitochondria

Mitochondria were isolated from HEK cells in the logarithmic growth phase, vitrified by plunge freezing, and imaged using VPP-CET. Due to the high density of the mitochondrial matrix in mammals, we mostly acquired tomograms of thin mitochondria, which had sufficient contrast for identification of mitoribosome particles with high specificity. Typically, imaged mitochondria measured approximately 200 nm along the beam direction and up to 800 nm in the perpendicular plane. In the reconstructed tomograms, mitoribosomes can be distinguished clearly from the mitochondrial matrix (Figure 1A).

To generate an unbiased template for subsequent automatic search, 231 subtomograms depicting putative mitoribosomes were interactively located in two tomograms and iteratively aligned using a sphere as an initial reference (Chen et al., 2013). The resulting subtomogram average is highly similar to cryo-EM SPA reconstructions of the mammalian mitoribosome (Figure S1A). This subtomogram average was used as a template for a six-dimensional cross-correlation search ("template matching") in 51 acquired tomograms (Lučić et al., 2005). Areas corresponding to peaks of the cross-correlation function were visually inspected to remove obvious false positives from the set of candidate particles, resulting in 7,796 subtomograms that were individually reconstructed and iteratively aligned. Using classification based on constrained principal component analysis (CPCA) (Förster et al., 2008) of the mitoribosome particles, false positives and low-quality particles were removed, resulting in 2,592 well-defined particles (Figure S1B). To identify mitoribosomes in a homogeneous state, the particles underwent a second round of CPCA classification, focusing on the small subunit (SSU) of the mitoribosome particles (Figure S1B). The class averages indicate that the SSU is present in all particles, but in approximately 10% of particles the SSU is less defined, probably due to structural variability. In total, 2,343 mitoribosome particles were retained for further analysis.

Most of the identified mitoribosomes appear to reside near the cristae or on the top and the bottom surface of the imaged mitochondria, all in close proximity to the IMM (Figure 1A). To quantify the spatial distribution, we computed the Euclidean distance between the center of detected mitoribosomes and the surface of the IMM for two representative tomograms. Indeed, the resulting distribution of distances suggests that the vast majority of mitoribosomes is directly adjacent to the IMM (Figure 1B), as also observed for the yeast mitoribosome (Pfeffer et al., 2015). The median distance between the center of the mitoribosome and the IMM is approximately 15 nm.

In our tomograms, mitoribosomes typically appear in clusters on the IMM. Ribosome particles that are engaged in translation of the same mRNA molecule (polysome) tend to adopt specific three-dimensional (3D) organizations (Brandt et al., 2010; Pfeffer et al., 2012, 2015). To analyze the 3D organization of human mitoribosomes, we determined the relative positions and orientations of its next neighbor within a maximum center-to-center distance of 40 nm. To exclude particles from different membranes from the analysis, we removed those pairs from the dataset that had a relative membrane inclination of more than 35° (Figures S2A and S2B). The plot of the relative positions and orientations of these neighbors yielded two distinct clusters (Figures S2C and S2D). When visualizing the arrangements represented by these two populations using the average positions and orientations, we observed that these clusters likely correspond to the left and the right neighbor within the same polysomal arrangement (Figure S2E).

This arrangement of mitoribosomes in a polysome results in a curved path of mRNA (Figure 1C). This arrangement minimizes unoccupied mRNA stretches, and we have previously observed it at the ER (Pfeffer et al., 2012) and also in yeast mitochondria (Pfeffer et al., 2015). However, compared with the 3D organization of yeast mitoribosomes (Pfeffer et al., 2015), the plot of relative positions and orientations shows less-defined clusters for human mitoribosomes. This indicates an increased variability of adjacent polysomal mitoribosomes or clusters of adjacent mitoribosomes not engaged in translation of the same mRNA molecule.

In Situ Structure of the Human Mitoribosome

The 2,343 subtomograms depicting well-defined mitoribosomes were subjected to a second round of classification focusing on the membrane region (Figure S1B), resulting in 663 particles with clear density for the IMM. This low proportion of particles with clear membrane density mainly results from the geometry of imaged mitochondria: the majority of particles reside at the top or the bottom of the flattened mitochondria ("top views"), where the mitochondrial membrane is not resolved due to the limited tilt range in CET ("missing wedge effect"). We decided to exclude these top views from further analysis, (1) because over-representation of one particular view in the dataset results in anisotropic resolution and artificial elongation of the averaged density along the imaging direction (as illustrated in Figure S1C) and (2) because including the top views resulted in only an insignificant improvement of the overall resolution, indicating that the sample and raw data quality rather than the particle number limit the obtainable resolution.

The remaining 663 subtomograms were iteratively aligned and averaged, resulting in a structure with well-defined SSU and large subunit (LSU) as well as pronounced density for the IMM (Figure 2A). Fourier shell cross-resolution against a cryo-EM single-particle reconstruction of the human mitoribosome (Amunts et al., 2015) (EMDataBank: EMD-2876) yielded a resolution of 25 Å (Fourier shell correlation [FSC] = 0.33). FSC of two independently aligned averages from each half of the data indicated a resolution of 26 Å (FSC = 0.143) (Figure S3). Local resolution varies between 22 and 28 Å for the mitoribosome and up to 34 Å for the peripheral membrane regions (Figure 2B).

For molecular interpretation, an atomic model of the human mitoribosome (PDB: 3j9m) was fitted into the subtomogram average (Figure 2C). Most of the density is explained well by the fitted atomic model. However, unexplained density is present in proximity to the head of the SSU. This uncovered density associates with mS39 (Figure 3A), which is positioned at the mRNA entry site of the SSU and supposedly guides the mRNA into the mitoribosomal mRNA channel (Greber et al., 2015). The size of the density suggests a mass of approximately 100 kDa. The resolution within this region is lower than for the core of the mitoribosome (Figure 2B), indicating compositional or conformational heterogeneity, which could not be disentangled using subtomogram classification (Figure S1B).

In the subtomogram average, membrane association of the human mitoribosome is mediated by a single contact site, which co-localizes with mL45 in the fitted atomic model (Figure 3B). Thus, similar to its yeast homolog Mba1 (Pfeffer et al., 2015), mL45 mediates the IMM association of the mammalian mitoribosome. Compared with the atomic model of the human mitoribosome (PDB: 3j9m), a larger part of the N-terminal domain of mL45 was modeled in the atomic model of the porcine mitoribosome (Greber et al., 2015) (PDB: 5Aj4); toward the C terminus of mL45 it contains an additional α helix h2 (S101-K114; considering a predicted, unresolved helix h1 from E53-K62). To analyze the interaction of mL45 with the membrane in detail, we thus

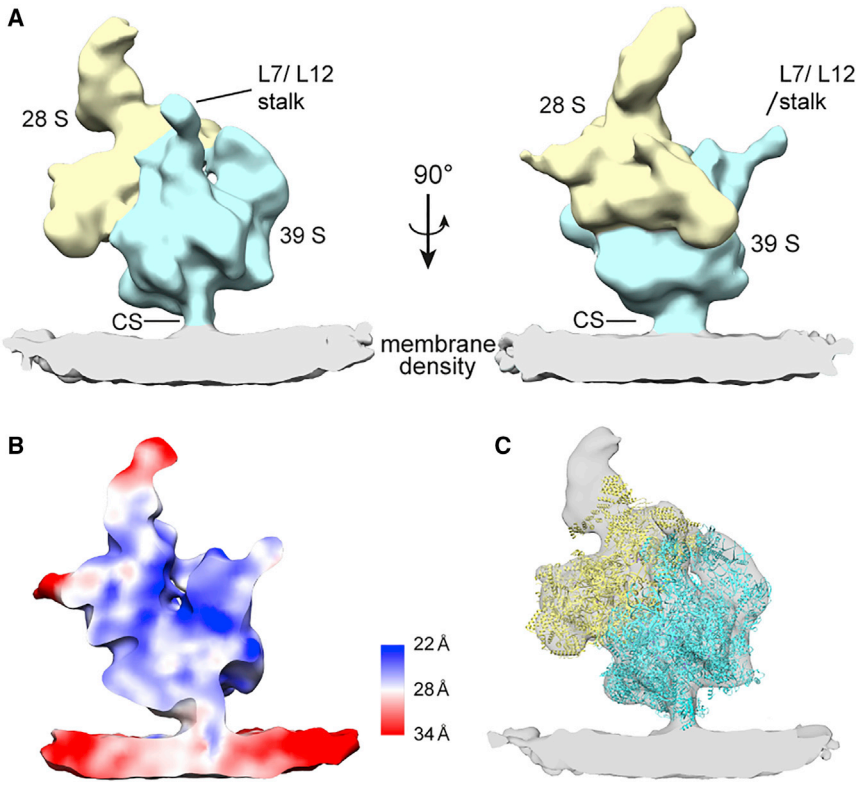

Figure 2. Structure of the Membrane-Bound Human Mitoribosome

(A) Subtomogram average of the human mitoribosome filtered to 25 Å (SSU, yellow; LSU, blue; IMM, gray). The contact site (CS) tethering the mitoribosome to the IMM is indicated.

(B) Local-resolution map.

(C) Atomic model of the human 55S mitoribosome (PDB: 3j9m) fitted into the subtomogram average.

See also Figures S1 and S3.

fitted the model of the porcine mitoribosome into the subtomogram average. h2 and h3 (V116-S128) of the fitted mL45 model are positioned directly on the membrane, suggesting that they mediate the interaction with the IMM (Figure 3B). Mitoribosomal membrane attachment by h2 of mL45 was already suggested previously (Greber et al., 2014) due to its positioning at the PET and the structural homology to the C-terminal domain of Tim44.

Comparison with the Yeast Mitoribosome

While the yeast mitoribosome associates with the IMM via two contacts, mediated by the mL45 homolog Mba1 and the long rRNA expansion segment 96-ES1, the *in situ* structure of the human mitoribosome reveals only one mL45-mediated contact site (Figure 4A). Thus, mitoribosomal proteins do not compensate for the absence of 96-ES1 in mammals. On both the human and yeast mitoribosome, mL45/Mba1 is positioned directly beneath the PET, bridging the ~30-Å gap between the ribosomal surface and the IMM (Figure 4A). Due to the strongly remodeled pathway of the PET in yeast, the absolute position of mL45/Mba1 on the mitoribosome differs between the human and yeast systems (Figure 4A), but with respect to the PET the position remains essentially invariant.

To analyze how the absence of the second contact site affects the arrangement of mitoribosome and membrane in humans, the subtomogram averages of the human and yeast mitoribosome (EMDataBank: EMD-2826) were aligned based on the conserved cores of their LSU rRNA (Figures 4B and S4A). The global arrangement of mitoribosome and membrane is defined by two main parameters: (1) the distance between the mitoribosomal core and the membrane surface, and (2) the orientation of the mitoribosome with respect to the IMM plane. The distance between a common reference point (ribosomal peptidyl-transferase center) and the surface of the IMM indicates that the catalytic core of the human mitoribosome resides approximately 15 Å closer to the membrane than that of the yeast mitoribosome (Figure 4B). This is in agreement with the decreased size of the human mitoribosome. The orientation of the mammalian mitoribosome core, however, is strikingly similar to that of the yeast mitoribosome: the orientations of the membrane planes differ by no more than approximately 5°.

The presence of only one major membrane association site for the human mitoribosome suggests that its relative orientation with respect to the membrane might be more flexible than for its yeast counterpart. Subtomogram classification focused on the membrane region of the average consistently yielded classes depicting a range of different membrane inclinations with respect to the mitoribosome. To analyze the flexibility of mitoribosome orientation with respect to the IMM, we fitted atomic models into these class averages as rigid bodies and determined the positions of three reference points (located on mL45, the SSU, and LSU) in a common coordinate system. Difference vectors between mL45 and the reference points on the SSU and LSU reveal orientation variability of the mitoribosome on the IMM (Figure S4B). Classes with maximal membrane inclination tilt approximately ±10° with respect to the average orientation (Figure S4B). High variability of mitoribosome association to the IMM is consistent with the decreasing local resolution observed for the membrane region of the subtomogram average and might also explain why polysomal mitoribosome arrangements are less defined in human mitochondria compared with yeast (Figure S2D).

DISCUSSION

In Situ Structure of the Human Mitoribosome

Here, we studied the structure and distribution of human mitoribosomes in their native microenvironment using CET and subtomogram analysis. By imaging intact human mitochondria, extensive purification procedures were circumvented and the IMM association of the mitoribosome was preserved. Comparison of the *in situ* subtomogram average with high-resolution

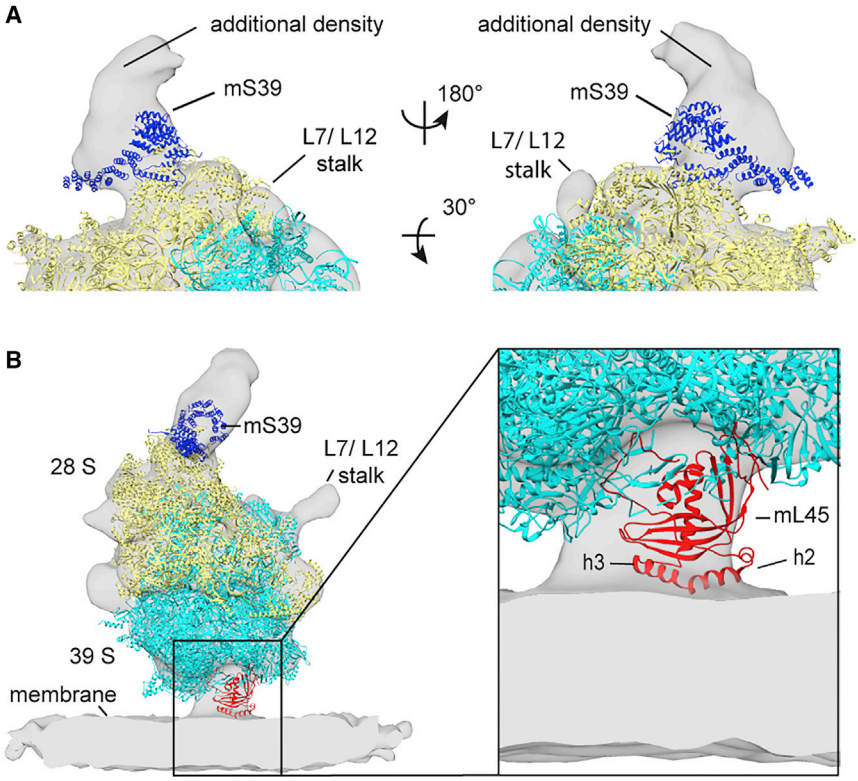

Figure 3. Features of the *In Situ* Mitoribosome Structure

(A) Density of roughly 100 kDa, unexplained by the atomic model near mS39 (dark blue).

(B) The mitoribosome is attached to the membrane via mL45 (red, PDB: 5aj4). Its amphipathic α-helices h2 and h3 are positioned on the membrane surface.

See also Figure S5.

structures of the isolated mitoribosome reveals an additional density on the small mitoribosomal subunit (Figure 3A). This density might represent a weakly bound cofactor, which dissociates upon solubilization and purification. The additional density associates with mS39, which forms parts of the ribosomal mRNA entry site and interacts with mitochondrial mRNAs (Davies et al., 2009). The spatial proximity between the unexplained density and mS39 as well as the mRNA channel may hint at its involvement in translation regulation.

Association with the Inner Mitochondrial Membrane

In our subtomogram average, membrane association of the 55S mitoribosome is mediated by only a single contact site, involving mL45 (Figure 3B). Fitting of the high-resolution structure of the isolated porcine mitoribosome suggests that the amphipathic helices h2 and h3 of mL45 establish contact with the IMM. The lipid composition of the mammalian IMM, mainly consisting of negatively charged cardiolipin and zwitterionic phosphatidylethanolamine (Daum, 1985), potentially supports electrostatic interactions of the helices h2 and h3, which contain several charged amino acids pointing toward the membrane surface (Figure S5). However, considering the high protein-to-lipid ratio of the IMM (3:1) (Daum, 1985), it cannot be ruled out that mL45 additionally interacts with membrane-embedded proteins that could not be resolved. A second contact site, which has previously been hypothesized to be mediated by the IMM proteins MPV17L2 or LetM1 (Mai et al., 2017) serving as ribosome recruitment factors (Dalla Rosa et al., 2014; Piao et al., 2009), was not observed. Consequently, MPV17L2 and LetM1 either must contribute to the mL45-mediated contact site or they associate only transiently during mitoribosome recruitment.

Another factor, which is likely to be involved in the visualized IMM contact site, is the membrane insertase Oxa1L. Its C-terminal domain was shown to bind to the ribosome (Haque et al., 2010; Keil et al., 2012; Szyrach et al., 2003), and the matrix-exposed loops of its bacterial homolog YidC serve functional roles in ribosome recruitment and subsequent protein insertion into the membrane (Geng et al., 2015). In the light of the large body of biochemical studies indicating cooperativity of Mba1 and Oxa1p in yeast (Keil et al., 2012; Lorenzi et al., 2016; Ott et al., 2006; Preuss et al., 2001; Szyrach et al., 2003) and the association of human mitoribosomes with Oxa1L (Haque et al., 2010; Richter-Dennerlein et al., 2016), it appears likely that Oxa1L is involved in the contact site. A higher-resolution *in situ* structure of the mitoribosome attached to the IMM could further clarify permanent and transient components of the co-translational insertion machinery and reveal their molecular architecture.

Evolution of Mitoribosomal Membrane Association

The conserved molecular architecture of the Mba1/mL45-mediated contact site suggests a general role for mL45 and its homologs in mitochondrial membrane protein biogenesis. Based on its position close to the mitoribosomal PET in yeast, Mba1 was previously proposed to guide the highly hydrophobic nascent polypeptides from the tunnel exit to the associated membrane protein insertase (Pfeffer et al., 2015), which was further supported by crosslinking experiments (Lorenzi et al., 2016). Interestingly, the C-terminal domain of Tim44, which is structurally related to mL45 (Greber et al., 2014), also was recently shown to directly interact with peptides during their translocation from the mitochondrial intermembrane space to the mitochondrial matrix (Banerjee et al., 2015). These findings, together with the identification of mL45 as the major constituent of the single contact site between mitoribosome and IMM, suggest a conserved role of the Mba1/mL45 contact site in peptide transfer. A systematic structural analysis of membrane-associated mitoribosomes from various evolutionarily distant mitochondria-containing organisms will have to show whether the molecular architecture of the Mba1/mL45-mediated contact site is indeed universally conserved. The investigation of

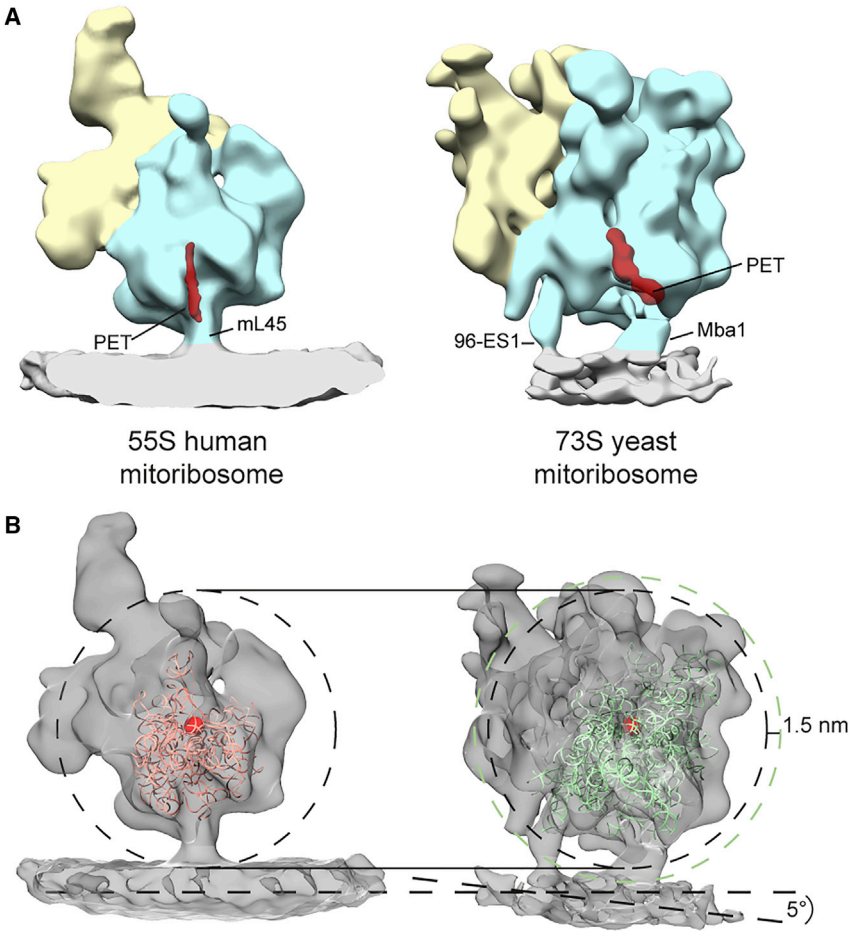

Figure 4. Comparison of IMM Interaction between the Human and the Yeast Mitoribosome

(A) *In situ* structures of the human and yeast mitoribosomes, with the contact sites and the peptide exit tunnel (PET, red) highlighted.

(B) *In situ* structures aligned to each other based on their LSU rRNA (PDB: 3J9M rRNA, salmon; PDB: 3J6B rRNA, green). Membrane planes are indicated by dashed lines and shown in the view with maximum tilt difference. Dashed circles (black, human; green, yeast) indicate distance between peptide translocation center (red sphere) and IMM. See also Figure S4.

additional contacts from an evolutionary perspective, such as the one formed by the expansion segment 96-ES1 in yeast, could provide clues about their function.

Our structure of the human mitoribosome, studied *in situ* using CET, reveals that the human mitoribosome shares a conserved IMM contact site with the yeast mitoribosome, despite the vast structural rearrangements throughout evolution. Still, many mechanistic details, in particular regarding the transfer of highly hydrophobic nascent polypeptides from the PET to the IMM and their subsequent membrane insertion as well as the precise molecular organization of membrane association, remain to be investigated. Recent advances in mitoribosome purification protocols (Couvillion et al., 2016) and electron microscopic imaging technology (Bai et al., 2015) provide promising tools to address these open questions in further detail in the future.

STAR★METHODS

Detailed methods are provided in the online version of this paper and include the following:

- KEY RESOURCES TABLE
- CONTACT FOR REAGENT AND RESOURCE SHARING
- EXPERIMENTAL MODEL AND SUBJECT DETAILS
- METHOD DETAILS
  - Isolation of Mitochondria from HEK Cells
  - Cryoelectron Tomography
  - Data Processing
  - Ribosome Distribution Analysis
  - Molecular Weight Estimation of the Extra Density
  - Analysis of the Flexibility of the Mitoribosome
- DATA AND SOFTWARE AVAILABILITY

SUPPLEMENTAL INFORMATION

Supplemental Information includes five figures and can be found with this article online at http://dx.doi.org/10.1016/j.str.2017.07.011.

AUTHOR CONTRIBUTIONS

R.E. prepared the sample, acquired tomography data, and, together with S.P. and F.F., carried out analysis of CET data. S.P. and F.F. planned and supervised the experiments and, together with R.E., wrote the manuscript.

ACKNOWLEDGMENTS

This work was supported by grants from the Deutsche Forschungsgemeinschaft to F.F. (FO 716/4-1 and the German Research Council GRK1721), as well as the Nederlandse Organisatie voor Wetenschappelijke Onderzoek (Vici 724.016.001). We thank Sabine Suppmann and Melanie Ried of the core facility of the Max Planck Institute of Biochemistry for suspension culture of HEK cells. The authors declare no competing financial interests.

Received: March 30, 2017
Revised: June 12, 2017
Accepted: July 26, 2017
Published: August 31, 2017

REFERENCES

Amunts, A., Brown, A., Bai, X., Llácer, J.L., Hussain, T., Emsley, P., Long, F., Murshudov, G., Scheres, S.H.W., and Ramakrishnan, V. (2014). Structure of the yeast mitochondrial large ribosomal subunit. Science *343*, 1485–1489.

Amunts, A., Brown, A., Toots, J., Scheres, S.H.W., and Ramakrishnan, V. (2015). Ribosome. The structure of the human mitochondrial ribosome. Science *348*, 95–98.

Bai, X., McMullan, G., and Scheres, S.H. (2015). How cryo-EM is revolutionizing structural biology. Trends Biochem. Sci. *40*, 49–57.

Banerjee, R., Gladkova, C., Mapa, K., Witte, G., and Mokranjac, D. (2015). Protein translocation channel of mitochondrial inner membrane and matrix-exposed import motor communicate via two-domain coupling protein. Elife *4*, e11897.

Berens, P. (2009). CircStat: a MATLAB toolbox for circular statistics. J. Stat. Softw. *31*, 1–21.

Brandt, F., Carlson, L.-A., Hartl, F.U., Baumeister, W., and Grünewald, K. (2010). The three-dimensional organization of polyribosomes in intact human cells. Mol. Cell *39*, 560–569.

Brown, A., Amunts, A., Bai, X., Sugimoto, Y., Edwards, P.C., Murshudov, G., Scheres, S.H.W., and Ramakrishnan, V. (2014). Structure of the large ribosomal subunit from human mitochondria. Science *346*, 718–722.

Cardone, G., Heymann, J.B., and Steven, A.C. (2013). One number does not fit all: mapping local variations in resolution in cryo-EM reconstructions. J. Struct. Biol. *184*, 226–236.

Chen, Y., Pfeffer, S., Hrabe, T., Schuller, J.M., and Förster, F. (2013). Fast and accurate reference-free alignment of subtomograms. J. Struct. Biol. *182*, 235–245.

Couvillion, M.T., Soto, I.C., Shipkovenska, G., and Churchman, L.S. (2016). Synchronized mitochondrial and cytosolic translation programs. Nature *533*, 499–503.

Danev, R., Buijsse, B., Khoshouei, M., Plitzko, J.M., and Baumeister, W. (2014). Volta potential phase plate for in-focus phase contrast transmission electron microscopy. Proc. Natl. Acad. Sci. USA *111*, 15635–15640.

Daum, G. (1985). Lipids of mitochondria. Biochim. Biophys. Acta *822*, 1–42.

Davies, S.M.K., Rackham, O., Shearwood, A.-M.J., Hamilton, K.L., Narsai, R., Whelan, J., and Filipovska, A. (2009). Pentatricopeptide repeat domain protein 3 associates with the mitochondrial small ribosomal subunit and regulates translation. FEBS Lett. *583*, 1853–1858.

Eibauer, M., Hoffmann, C., Plitzko, J.M., Baumeister, W., Nickell, S., and Engelhardt, H. (2012). Unraveling the structure of membrane proteins in situ by transfer function corrected cryo-electron tomography. J. Struct. Biol. *180*, 488–496.

Förster, F., Pruggnaller, S., Seybert, A., and Frangakis, A.S. (2008). Classification of cryo-electron sub-tomograms using constrained correlation. J. Struct. Biol. *161*, 276–286.

Geng, Y., Kedrov, A., Caumanns, J.J., Crevenna, A.H., Lamb, D.C., Beckmann, R., and Driessen, A.J.M. (2015). Role of the cytosolic loop C2 and the C terminus of YidC in ribosome binding and insertion activity. J. Biol. Chem. *290*, 17250–17261.

Greber, B.J., Boehringer, D., Leitner, A., Bieri, P., Voigts-Hoffmann, F., Erzberger, J.P., Leibundgut, M., Aebersold, R., and Ban, N. (2014). Architecture of the large subunit of the mammalian mitochondrial ribosome. Nature *505*, 515–519.

Greber, B.J., Bieri, P., Leibundgut, M., Leitner, A., Aebersold, R., Boehringer, D., and Ban, N. (2015). Ribosome. The complete structure of the 55S mammalian mitochondrial ribosome. Science *348*, 303–308.

Haque, M.E., Elmore, K.B., Tripathy, A., Koc, H., Koc, E.C., and Spremulli, L.L. (2010). Properties of the C-terminal tail of human mitochondrial inner membrane protein Oxa1L and its interactions with mammalian mitochondrial ribosomes. J. Biol. Chem. *285*, 28353–28362.

Hell, K., Neupert, W., and Stuart, R.A. (2001). Oxa1p acts as a general membrane insertion machinery for proteins encoded by mitochondrial DNA. EMBO J. *20*, 1281–1288.

Hrabe, T., Chen, Y., Pfeffer, S., Cuellar, L.K., Mangold, A.-V., and Förster, F. (2012). PyTom: a python-based toolbox for localization of macromolecules in cryo-electron tomograms and subtomogram analysis. J. Struct. Biol. *178*, 177–188.

Keil, M., Bareth, B., Woellhaf, M.W., Peleh, V., Prestele, M., Rehling, P., and Herrmann, J.M. (2012). Oxa1-ribosome complexes coordinate the assembly of cytochrome C oxidase in mitochondria. J. Biol. Chem. *287*, 34484–34493.

Khoshouei, M., Pfeffer, S., Baumeister, W., Förster, F., and Danev, R. (2017). Subtomogram analysis using the Volta phase plate. J. Struct. Biol. *197*, 94–101.

Kremer, J.R., Mastronarde, D.N., and McIntosh, J.R. (1996). Computer visualization of three-dimensional image data using IMOD. J. Struct. Biol. *116*, 71–76.

Lorenzi, I., Oeljeklaus, S., Ronsör, C., Bareth, B., Warscheid, B., Rehling, P., and Dennerlein, S. (2016). Ribosome-associated Mba1 escorts Cox2 from insertion machinery to maturing assembly intermediates. Mol. Cell. Biol. *36*, 2782–2793.

Lučić, V., Förster, F., and Baumeister, W. (2005). Structural studies by electron tomography: from cells to molecules. Annu. Rev. Biochem. *74*, 833–865.

Mai, N., Chrzanowska-Lightowlers, Z.M.A., and Lightowlers, R.N. (2017). The process of mammalian mitochondrial protein synthesis. Cell Tissue Res. *367*, 5–20.

Mastronarde, D.N. (2005). Automated electron microscope tomography using robust prediction of specimen movements. J. Struct. Biol. *152*, 36–51.

Nickell, S., Förster, F., Linaroudis, A., Net, W.D., Beck, F., Hegerl, R., Baumeister, W., and Plitzko, J.M. (2005). TOM software toolbox: acquisition and analysis for electron tomography. J. Struct. Biol. *149*, 227–234.

Ott, M., and Herrmann, J.M. (2010). Co-translational membrane insertion of mitochondrially encoded proteins. Biochim. Biophys. Acta *1803*, 767–775.

Ott, M., Prestele, M., Bauerschmitt, H., Funes, S., Bonnefoy, N., and Herrmann, J.M. (2006). Mba1, a membrane-associated ribosome receptor in mitochondria. EMBO J. *25*, 1603–1610.

Pettersen, E.F., Goddard, T.D., Huang, C.C., Couch, G.S., Greenblatt, D.M., Meng, E.C., and Ferrin, T.E. (2004). UCSF Chimera—a visualization system for exploratory research and analysis. J. Comput. Chem. *25*, 1605–1612.

Pfeffer, S., Brandt, F., Hrabe, T., Lang, S., Eibauer, M., Zimmermann, R., and Förster, F. (2012). Structure and 3D arrangement of endoplasmic reticulum membrane-associated ribosomes. Structure *20*, 1508–1518.

Pfeffer, S., Woellhaf, M.W., Herrmann, J.M., and Förster, F. (2015). Organization of the mitochondrial translation machinery studied in situ by cryoelectron tomography. Nat. Commun. *6*, 6019.

Piao, L., Li, Y., Kim, S.J., Byun, H.S., Huang, S.M., Hwang, S.-K., Yang, K.-J., Park, K.A., Won, M., Hong, J., et al. (2009). Association of LETM1 and MRPL36 contributes to the regulation of mitochondrial ATP production and necrotic cell death. Cancer Res. *69*, 3397–3404.

Preuss, M., Leonhard, K., Hell, K., Stuart, R.A., Neupert, W., and Herrmann, J.M. (2001). Mba1, a novel component of the mitochondrial protein export machinery of the yeast *Saccharomyces cerevisiae*. J. Cell Biol. *153*, 1085–1096.

Richter-Dennerlein, R., Oeljeklaus, S., Lorenzi, I., Ronsör, C., Bareth, B., Schendzielorz, A.B., Wang, C., Warscheid, B., Rehling, P., Dennerlein, S., et al. (2016). Mitochondrial protein synthesis adapts to influx of nuclear-encoded protein. Cell *167*, 471–483.e10.

Dalla Rosa, I., Durigon, R., Pearce, S.F., Rorbach, J., Hirst, E.M.A., Vidoni, S., Reyes, A., Brea-Calvo, G., Minczuk, M., Woellhaf, M.W., et al. (2014).

MPV17L2 is required for ribosome assembly in mitochondria. Nucleic Acids Res. *42*, 8500–8515.

Scheres, S.H.W. (2012). RELION: implementation of a Bayesian approach to cryo-EM structure determination. J. Struct. Biol. *180*, 519–530.

van der Sluis, E.O., Bauerschmitt, H., Becker, T., Mielke, T., Frauenfeld, J., Berninghausen, O., Neupert, W., Herrmann, J.M., and Beckmann, R. (2015). Parallel structural evolution of mitochondrial ribosomes and OXPHOS complexes. Genome Biol. Evol. *7*, 1235–1251.

Szyrach, G., Ott, M., Bonnefoy, N., Neupert, W., and Herrmann, J.M. (2003). Ribosome binding to the Oxa1 complex facilitates co-translational protein insertion in mitochondria. EMBO J. *22*, 6448–6457.

STAR★METHODS

KEY RESOURCES TABLE

REAGENT or RESOURCE	SOURCE	IDENTIFIER
Chemicals, Peptides, and Recombinant Proteins		
FreeStyle™ 293 Expression Medium	ThermoFisher	CAT# 12338018
EGTA	Sigma-Aldrich	CAT# E8145-10G
Deposited Data		
Structure of the membrane-bound human mitoribosome (electron density map)		EMD-3784
Experimental Models: Cell Lines		
HEK-293E	Y. Durocher *et al.*, NAR Vol. 30 pp2-9, 2002	
Software and Algorithms		
SerialEM	Mastronarde, 2005	N/A
IMOD	Kremer et al., 1996	N/A
Chimera	Pettersen et al., 2004	N/A
Pytom	Hrabe et al., 2012	N/A
TOM Toolbox	Nickell et al., 2005	N/A
Bsoft software package	Cardone et al., 2013	N/A
Other		
Quantifoil holey carbon coated copper grids (R 2/1)	Quantifoil	N/A

CONTACT FOR REAGENT AND RESOURCE SHARING

Further information and requests for resources and reagents should be directed to and will be fulfilled by the Lead Contact, Friedrich Förster (f.g.forster@uu.nl).

EXPERIMENTAL MODEL AND SUBJECT DETAILS

HEK cells were grown in suspension to a cell density of 1.1 x10^6/ ml at 37°C in FreeStyle™ 293 Expression Medium (ThermoFisher), pelleted at 600g and washed once with PBS. Cell viability was determined to 98.4% by trypan blue staining.

METHOD DETAILS

Isolation of Mitochondria from HEK Cells

All subsequent steps were performed at 4° C. The cell pellet from 1 Liter of cell culture was resolved in 15 ml of isolation buffer (10 mM Tris, 150 mM sucrose, 1 mM EGTA, pH 7.4) and homogenized in a Potter-Elvehjem homogenizer for 10 minutes at 1,200 rpm by continuous up- and downstrokes. The resulting lysate was centrifuged for 10 minutes at 800 g, the supernatant was collected and centrifuged at 9,000 g for 10 minutes. The resulting supernatant was decanted and the pellet washed once with buffer, prior to a last centrifugation step at 9,000 g for 10 minutes. The supernatant was discarded and the final pellet was resuspended in 1.5 ml of isolation buffer, aliquoted and flash-frozen in liquid nitrogen. The samples were stored at -80°C.

Cryoelectron Tomography

Quantifoil holey carbon coated copper grids (R 2/1) were glow discharged for 60 seconds before 3 μl of diluted mitochondria were applied to the grid and mixed with 3μl gold fiducial markers in 10mM Tris, pH 7.4 by pipetting. Grids were then manually blotted with filter paper from the back for 3 seconds and plunged into a liquid ethane-propane mixture using a custom-built guillotine plunger. The grids were mounted on autogrids (FEI). Tiltseries were recorded on a FEI Titan Krios operated at 300 kV equipped with the Volta Phase Plate, a Gatan K2 summit direct electron detector (3838x3710 pixel) and a Gatan Quantum Imaging Filter. For each half of a tiltseries (0° to -60° and 2° to +60°, respectively, with an increment of 2°), a new position on the phase plate was used, which was pre-irradiated with 30 nC on a trial area prior to data acquisition (Danev et al., 2014). The pixel size corresponded to 2.62 Å on the specimen level and the nominal defocus was set to 500 nm (26 tiltseries) or 3 μm (25 tiltseries). The electron dose did not exceed 100 $e^-/Å^2$ per tiltseries. Data acquisition was performed with the SerialEM software (Mastronarde, 2005).

Data Processing

Tiltseries were aligned based on the fiducial markers using the TOM toolbox in MATLAB (Nickell et al., 2005). For tomograms with an insufficient number of gold markers, tilt image alignment was performed by patch tracking with the IMOD software package (Kremer et al., 1996). For the projections acquired at 3 μm defocus, phase reversals due to the contrast transfer function (CTF) were corrected using MATLAB scripts and PyTom (Hrabe et al., 2012) on single projections by strip-based periodogram averaging (Eibauer et al., 2012), accounting for a cosine shaped CTF as an effect of the phase plate. The aligned and weighted projections were downscaled in Fourier space from 3696x3696 to 462x462 pixels and tomograms were reconstructed in TOM (resulting voxel size 2.096 nm). Using reference-free spherical harmonics based subtomogram alignment (Chen et al., 2013) an initial structure for template matching was generated from 231 manually selected particles from two tomograms. To localize particles automatically in the complete set of tomograms template matching was performed with this reference using PyTOM (Hrabe et al., 2012). Peaks of the resulting 6-D cross-correlation function localized in the mitochondrial matrix were manually inspected in UCSF Chimera (Pettersen et al., 2004) to discard false-positive matches. For the retained coordinates, subtomograms were individually reconstructed (voxel size 0.524 nm) and subjected to subtomogram alignment using rotation sampling in real space with PyTom. Aligned subtomograms were classified using constrained principle component analysis (Förster et al., 2008) in PyTOM and TOM to enrich subtomograms with clear density for the IMM and the small ribosomal subunit (SSU). The subtomograms were then iteratively aligned until convergence in PyTOM using a gold-standard procedure (two independent half-sets) (Scheres, 2012). Resolution of the subtomogram average was determined by Fourier shell cross-resolution against a cryo-EM single particle reconstruction of the human mitochondrial ribosome (EMDataBank: EMD-2876, FSC = 0.33) and half-set resolution (FSC = 0.143). For local resolution estimation the Bsoft software package was used (Cardone et al., 2013).

Ribosome Distribution Analysis

For analyzing the distribution of distances between located mitoribosomes and the membrane, the outer and inner mitochondrial membranes of two tomograms were segmented with Amira (FEI) (voxel size of 2.1 nm). The Euclidean distance between the centres of mass of 155 classified mitoribosomes and the IMM was calculated in MATLAB (Mathworks, USA). The 3D distribution analysis was carried out as previously described for the yeast mitoribosome (Pfeffer et al., 2015). In brief, the coordinate system of the mitoribosome was chosen such that the IMM was perpendicular to the z-axis. The analysis was restricted to the neighbourhood of the 2,343 mitoribosomes obtained after two rounds of classification described in Figure S1. The next-neighbour analysis was restricted to only the next neighbour within a distance of 20 nm to 40 nm and a relative membrane inclination of 0 to 35°. Two angles describing the relative position (α) and orientation (β) of the next neighbour were defined (Figure S2C), plotted against each other and hierarchically clustered in these two dimensions in MATLAB using the 'single' linkage and 'distance' clustering criteria. For each cluster, the average positions, determined using spherical coordinates and the CircStat toolbox (Berens, 2009), and the average orientations were used for generating the polysome models.

Molecular Weight Estimation of the Extra Density

The density of the subtomogram average was determined by manually removing the membrane density, measuring the volume in UCSF chimera at the same density threshold depicted in the figures and normalizing it to the 2.7 MDa of the 55 S mitoribosome. The density was determined to 0.61 Da/ A^3. The extra density was then manually segmented, its volume measured at the same density threshold as the subtomogram average and the mass was determined to 110 kDa by using the determined density.

Analysis of the Flexibility of the Mitoribosome

The 909 subtomograms with a clear membrane-density, obtained after focused classification with a spherical mask and a mask encompassing the SSU (Figure S1), were separated into 17 classes with varying membrane inclinations. The atomic model of the 55S mitoribosome (PDB3j9m) was fitted into the class averages with UCSF Chimera's "Fit in Map" function. Reference points were chosen on the small (uS2m, L293) and large subunits (mL38, E181) and the membrane contact (mL45, Q119) in the atomic model (3j9m) with Chimeras Volume Tracer. The coordinates of the markers were then extracted and difference vectors between the membrane contact and the reference points on the small and large subunit were calculated in MATLAB. The average reference point positions were determined using spherical coordinates and the resulting vectors were used as reference to calculate the angular distance of each class. Rotation matrices describing the transformation between the average reference point positions and the maximum outlier positions - for which only the two thirds of datapoints with the smallest angular distance was considered - were determined in MATLAB (vrrotvec, vrrotvec2mat) and applied to the subtomogram average using TOM (tom_rotate) for the purpose of visualization (Figure S4B).

DATA AND SOFTWARE AVAILABILITY

A subtomogram average of the membrane-associated human mitoribosome has been deposited in the EMDataBank with accession code EMD-3784. All remaining relevant data are available from the authors. Correspondence and requests for data should be addressed to FF (f.g.forster@uu.nl).